

# Long-Lived Circular Rydberg Qubits of Alkaline-Earth Atoms in Optical Tweezers

C. Hölzl<sup>1</sup>, A. Götzelmann<sup>1</sup>, E. Pultinevicius<sup>1</sup>, M. Wirth<sup>1</sup>, and F. Meinert<sup>1</sup>

<sup>1</sup>*Physikalisches Institut and Center for Integrated Quantum Science and Technology, Universität Stuttgart, Pfaffenwaldring 57, 70569 Stuttgart, Germany*

(Dated: March 5, 2024)

Coherence time and gate fidelities in Rydberg atom quantum simulators and computers are fundamentally limited by the Rydberg state lifetime. Circular Rydberg states are highly promising candidates to overcome this limitation by orders of magnitude, as they can be effectively protected from decay due to their maximum angular momentum. We report the first realization of alkaline-earth circular Rydberg atoms trapped in optical tweezers, which provide unique and novel control possibilities due to the optically active ionic core. Specifically, we demonstrate creation of very high- $n$  ( $n = 79$ ) circular states of  $^{88}\text{Sr}$ . We measure lifetimes as long as 2.55 ms at room temperature, which are achieved via cavity-assisted suppression of black-body radiation. We show coherent control of a microwave qubit encoded in circular states of nearby manifolds, and characterize the qubit coherence time via Ramsey and spin-echo spectroscopy. Finally, circular state tweezer trapping exploiting the  $\text{Sr}^+$  core polarizability is quantified via measurements of the trap-induced light shift on the qubit. Our work opens routes for quantum simulations with circular Rydberg states of divalent atoms, exploiting the emergent toolbox associated with the optically active core ion.

## I. INTRODUCTION

Arrays of individually controlled and interacting Rydberg atoms based on optical tweezer technology have recently enabled rapid advances in the development of neutral atom quantum simulators and computers [1]. Prominent examples range from large scale simulation of quantum spin models [2, 3], over the implementation of optimization problems [4, 5], to high-fidelity gate operations in quantum circuits [6, 7], and even demonstrations of key steps towards quantum error correction [8–12].

For all these applications, the lifetime of the highly excited Rydberg levels sets a fundamental limit for achievable coherence times or gate fidelities. In this context, the use of circular Rydberg states has recently attracted increasing attention to overcome this constraint, both for analog quantum simulators and gate-based quantum computers [13, 14]. Circular Rydberg states have maximum allowed angular momentum (i.e.  $|m| = n - 1$ , where  $m$  and  $n$  denote the orbital magnetic and principal quantum number), which inhibits optical decay to low-lying orbitals by selection rules [15]. This opens up exciting prospects to increase the coherence time of Rydberg atom arrays by orders of magnitude either in cryogenic or room temperature setups [16–18]. Only very recently, first tweezer arrays with circular Rydberg states of rubidium atoms have been demonstrated using optical bottle beam traps [19].

In this article, we demonstrate the first tweezer-trapped circular states of alkaline-earth atoms, which in contrast to alkali atoms provide a second optically active electron. Combining the richer low-lying electronic structure of divalent atoms with atom arrays already gave rise to powerful new tools [20–22], for example for optical clock metrology or neutral atom quantum computing [23–26]. In contrast to low angular momentum Rydberg states (e.g. S- or D-orbitals), circular states of alkaline-earth atoms allow for ionic core excitation in

the absence of rapid autoionization, providing a plethora of unique possibilities. First, the ion core enables conservative trapping in standard Gaussian beam tweezers, which brings scaling advantages in view of power requirements when compared to the bottle traps needed for alkali-atoms. Second, photon scattering at the broad and narrow core transitions can be exploited for direct laser cooling and imaging of the trapped Rydberg atoms, making use of central manipulation techniques developed for trapped ions. Third, combining microwave control of the Rydberg electron with narrow-line optical core spectroscopy involving the ion's D-level enables local control and read-out of the circular Rydberg qubit via the quadrupole interaction between the two electrons (the latter was recently demonstrated in an atomic beam experiment [27]).

Here, we create very high- $n$  ( $n = 79$ ) circular Rydberg states of  $^{88}\text{Sr}$  atoms from an array of optical tweezers and demonstrate coherent control of a qubit encoded in circular states separated by two principal quantum numbers which is driven by a two-photon microwave (MW) transition. We demonstrate trapping of the circular Rydberg atom in the optical tweezer exploiting the dominating  $\text{Sr}^+$  core polarizability and analyze the effect of the trapping light on the qubit coherence. We observe lifetimes of the circular Rydberg states as long as 2.55 ms, which is about an order of magnitude longer than the free-space black-body decay at room temperature. The long lifetime is achieved by placing the atoms inside a pair of optically transparent capacitor plates, which suppress the black-body field at microwave frequencies.

## II. PREPARING CIRCULAR RYDBERG STATES

Our experiments start with an array of ten optical tweezers at a wavelength of  $\lambda = 539.91$  nm and a waist

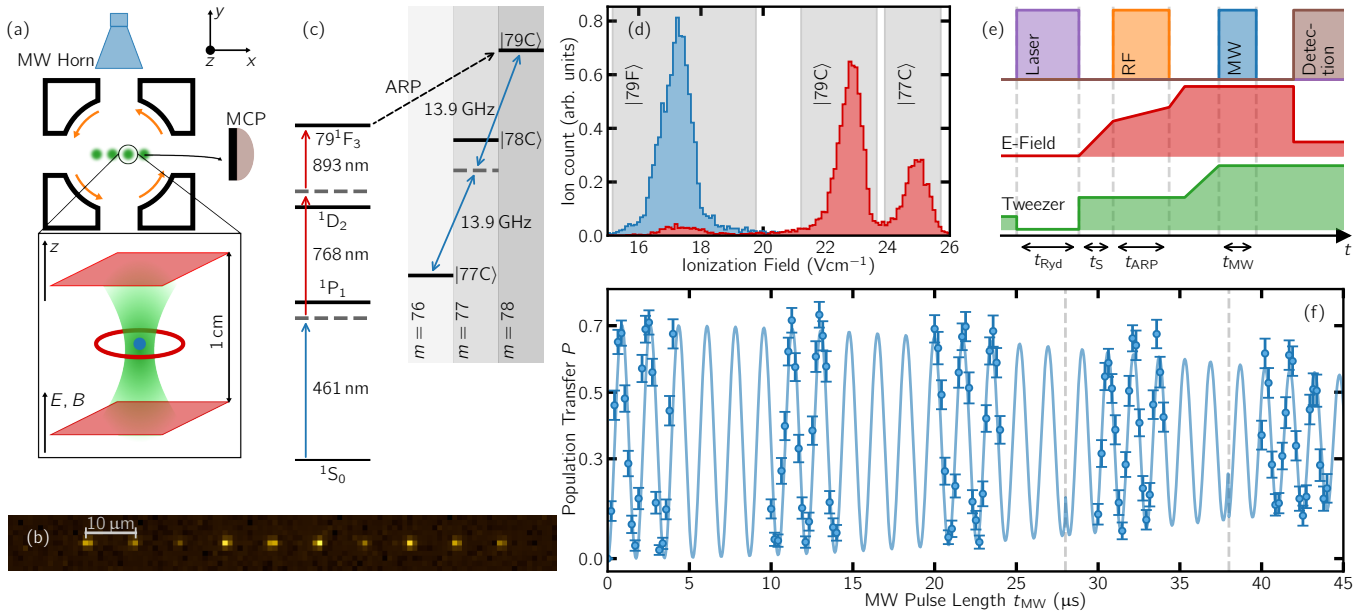


FIG. 1. (a) Schematic drawing of the experiment: Single  $^{88}\text{Sr}$  atoms are trapped in optical tweezers (green) inside an electrode structure consisting of two transparent electrodes (red) and four circularly shaped electrodes for applying  $\sigma^+$ -polarized RF fields (indicated with orange arrows). Magnetic and electric control fields  $E$  and  $B$  are aligned with the tweezer axis. (b) Averaged fluorescence image of single atoms in the ten tweezer array used throughout this work obtained through the transparent electrodes. (c) The atoms are excited to the  $|79F, m=2\rangle$  state via an off-resonant three-photon transition, from where they are transferred to the  $|79C\rangle$  circular Rydberg state by an adiabatic rapid passage (ARP). The qubit is implemented by coherently coupling  $|79C\rangle$  to  $|77C\rangle$  by two microwave photons at  $\approx 13.9$  GHz. (d) State-selective field ionization profile of the  $|79F\rangle$ ,  $|79C\rangle$  and  $|77C\rangle$  states ionized by a  $10\ \mu\text{s}$  linear field ramp to  $27(5)\ \text{Vcm}^{-1}$  before (blue) and after circularization and a partial transfer to  $|77C\rangle$  (red). The three states are well distinguishable and by counting the events within the gray integration windows, the state populations  $p_n$  are extracted. (e) Sketch of the experimental sequence showing tweezer trap depth (green), electric control field strength (red), Rydberg laser light (purple), RF field (orange), microwave for qubit control (blue), and state read-out via SSFI (brown). The employed technical components in (a) are colored accordingly. (f) Rabi oscillations on the  $|79C\rangle \leftrightarrow |77C\rangle$  microwave transition. The population transfer  $p_{77}/(p_{77} + p_{79})$  to find the atom in  $|77C\rangle$  as a function of the microwave pulse length  $t_{\text{MW}}$  is shown. The solid blue line is a sinusoidal fit with a Gaussian decay envelope. Note that for the three areas separated by the gray-dashed lines, the frequency is varied independently due to microwave power fluctuations between measurements.

of  $564(5)\ \text{nm}$ , which are stochastically loaded with single  $^{88}\text{Sr}$  atoms, cooled close to the motional ground state. (see Fig. 1(a) and (b); for details on tweezer loading, in-trap laser cooling, and parity projection in our setup, see Ref. [28]). The atoms are prepared inside a structure consisting of six electrodes. Four of them form a ring structure and allow us to apply electric fields in the  $x$ - $y$  plane of the tweezer array. The remaining two plate electrodes are placed below and above this ring structure for controlling the electric field along the  $z$ -direction (direction of axial tweezer confinement). They are fabricated from glass coated with a thin film ( $\approx 700\ \text{nm}$  thickness) of indium tin oxide (ITO) [17], which grants excellent optical access for laser cooling, high-NA tweezer generation, and single-atom imaging.

We prepare circular Rydberg states (CRS) by first exciting the atoms from the  $1S_0$  ground state to the  $n=79, 1F_3, m=2$  Rydberg level in the presence of a magnetic field  $B=0.40(5)\ \text{G}$  pointing along the  $z$ -direction (see Fig. 1(a)) [29]. During this  $t_{\text{Ryd}}=20\ \mu\text{s}$  long off-

resonant three-photon excitation (*cf.* Fig. 1(e)), the tweezer light is turned off to prevent light shifts. Subsequently, the electron is transferred into the circular Rydberg orbit  $|79C\rangle$  ( $n=79, l=m=78$ ) via an adiabatic rapid passage protocol. To this end, we first ramp up the electric field along  $z$  from zero to  $E=478(1)\ \text{mVcm}^{-1}$  within  $t_S=5\ \mu\text{s}$ . At this field the initial Rydberg F-state smoothly attaches to the Stark-shifted manifold of high- $l$  levels, effectively forming an equidistant ladder of states with increasing  $m$  up to the circular state. This allows for resonant coupling of all levels in that ladder with a single  $\sigma^+$ -polarized radio-frequency (RF) field. In our setup, we generate this field by applying sinusoidal voltages with frequency  $f_{\text{RF}}=70\ \text{MHz}$  and phase shifts of about  $90$  degrees between pairs of neighboring electrodes on the four ring electrodes. The adiabatic passage is then driven by slowly (within  $t_{\text{ARP}}=20\ \mu\text{s}$ ) sweeping the electric field along  $z$  further up to  $597(1)\ \text{mVcm}^{-1}$  through the RF-induced multi-level avoided crossing (see Appendix A for details). Note that prior to this work, circularization via

rapid adiabatic transfer has been explored for Rydberg states of much lower principal quantum number ( $n \leq 52$ ) [30].

We exploit state-selective ramped field ionization (SSFI) for ensemble-averaged state read-out. The ionization field is applied along the  $x$ -direction via two of the ring electrodes and guides the produced ions towards a microchannel plate (MCP) mounted outside the electrode cage for detection. Fig. 1(d) shows histograms of the ionization fields derived from the time-of-flight to the detector before and after the adiabatic rapid passage. For the data after transfer, we apply a resonant two-photon MW pulse which partially transfers  $|79C\rangle$  to  $|77C\rangle$ , as discussed in more detail in the next paragraph. SSFI provides powerful means to tell apart low- $l$  and high- $l$  states, but does not give enough resolution to distinguish the target circular Rydberg level from not fully stretched 'elliptical states' with  $l < n - 1$ . In order to probe the fidelity for preparing  $|79C\rangle$ , we implement coherent driving of a microwave qubit encoded in the circular Rydberg levels  $|79C\rangle$  and  $|77C\rangle$ , which are well separated in the SSFI signal (*cf.* Fig. 1(d)), from which the population  $p_{77}$  ( $p_{79}$ ) in  $|77C\rangle$  ( $|79C\rangle$ ) is extracted. Coupling the qubit states is achieved by an off-resonant two-photon microwave drive at  $f_{\text{MW}} = 13.86$  GHz (see Fig. 1(c)). Moreover, after the adiabatic passage and prior to the MW pulse, the electric field is ramped up to approximately  $2 \text{ Vcm}^{-1}$ , which shifts transitions from  $|79C\rangle$  to states other than  $|77C\rangle$  out of resonance. Recording the population transfer  $P = p_{77}/(p_{79} + p_{77})$  from  $|79C\rangle$  to  $|77C\rangle$  as a function of MW pulse length  $t_{\text{MW}}$  reveals coherent Rabi oscillations as depicted in Fig. 1(f). From the maximum population transfer into  $|77C\rangle$  after a  $\pi$ -pulse (i.e. after  $t_{\text{MW}} = 870(5)$  ns), we infer about  $\epsilon_{\text{CRS}} \approx 70\%$  preparation efficiency of the  $|79C\rangle$  circular Rydberg level. Damping of the Rabi oscillations is attributed to small shot-to-shot fluctuations of the microwave amplitude at the position of the atoms. It is well modeled by a Gaussian envelope [6], from which we extract an  $1/e$ -time of  $60(3) \mu\text{s}$ . Note that the Rabi frequency also changed by  $\approx 10\%$  between measurement sets due to fluctuations of the output power of the microwave generator. This is accounted for by fitting a function with piecewise independent frequencies in the areas separated by the gray-dashed lines.

### III. CIRCULAR STATE QUBIT COHERENCE

In a next step, we probe the transverse coherence time of the circular state qubit,  $|77C\rangle \leftrightarrow |79C\rangle$ , via its free induction decay. An exemplary dataset obtained from a standard Ramsey measurement ( $\pi/2$ -pulse, wait time  $t_{\text{R}}$ ,  $\pi/2$ -pulse) with a  $\pi/2$ -pulse time of  $t_{\pi/2} = 227(2)$  ns is shown in Fig. 2(a) (blue circles). A sinusoidal fit of the Ramsey signal with a Gaussian envelope  $\propto \exp(-t_{\text{R}}^2/2T_2^{*2})$ , reflecting a stochastic dephasing process from fluctuations of the qubit resonance frequency,

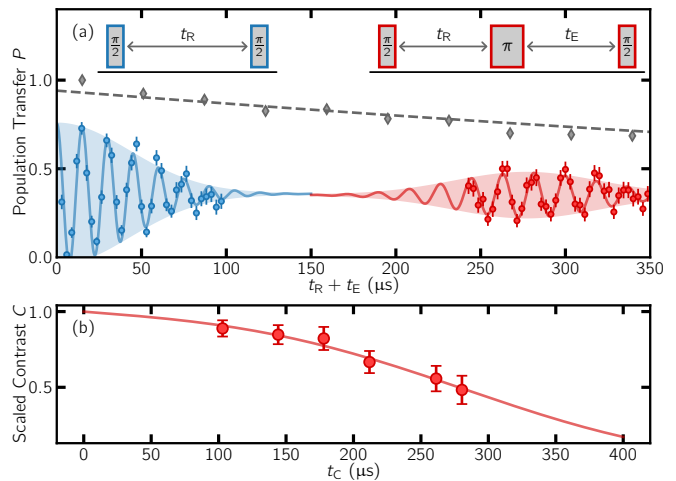


FIG. 2. (a) Measurement of the circular state qubit coherence via Ramsey (blue) and spin-echo (red) experiments. The population transfer  $P$  into the  $|77C\rangle$  state is plotted against the cumulative Ramsey time and echo time  $t_{\text{R}} + t_{\text{E}}$ . The microwave pulse sequences for Ramsey and spin-echo experiments are shown schematically above the data. Solid lines are Gaussian-damped sine functions fitted to the data. The gray diamonds show the combined ion detection probability in  $|79C\rangle$  and  $|77C\rangle$  ( $p_{77} + p_{79}$ ) scaled by the first data point. An exponential fit (gray-dashed line) to the data reveals a population lifetime in the qubit subspace of  $1.3(1)$  ms. (b) Maximum fringe contrast of the spin-echo signal, scaled by the preparation efficiency  $\epsilon_{\text{CRS}}$ , as a function of the revival time  $t_{\text{C}}$ . The solid line shows a fit of Eq. (1) to the data. Error bars show one standard deviation.

reveals a reversible coherence time  $T_2^* = 43(2) \mu\text{s}$ . In fact, during this time, longitudinal decay out of the qubit subspace is comparatively small (gray diamonds in Fig. 2(a)), and decoherence is primarily attributed to the first-order magnetic and second-order electric sensitivity of the transition between the circular states (see Appendix B for details). From the oscillation frequency of the Ramsey fringes, we deduce a MW (red) detuning of  $\Delta = 66.5(2)$  kHz.

Extending the Ramsey measurement to spin-echo interferometry ( $\pi/2$ -pulse, wait time  $t_{\text{R}}$ ,  $\pi$ -pulse, wait time  $t_{\text{E}}$ ,  $\pi/2$ -pulse) allows us to probe reversibility of the qubit dephasing. An exemplary dataset, for which we apply the echo  $\pi$ -pulse after  $t_{\text{R}} = 160 \mu\text{s}$  and scan  $t_{\text{E}}$ , is shown in Fig. 2(a) (red circles). A clear reappearance of fringes in the coherent qubit evolution is observed near  $t_{\text{E}} \approx t_{\text{R}}$ . We define the revival time  $t_{\text{C}}$  as the time where the contrast is maximal. Notably,  $t_{\text{C}}$  of the spin-echo is shifted from  $2t_{\text{R}}$  to earlier times (see Appendix B). From such measurements, we quantify the degree of reversibility by extracting the contrast at  $t_{\text{C}}$  from a sinusoidal fit to the data with a Gaussian envelope function. Fig. 2(b) depicts this contrast, scaled by the CRS preparation efficiency  $\epsilon_{\text{CRS}}$ , as a function of  $t_{\text{C}}$ . These measurements reveal coherent qubit evolution up to several hundred picoseconds, a timescale for which population loss out of

the qubit subspace cannot be fully ignored anymore. For this reason, we model the decay of the echo contrast with a functional form which also includes longitudinal decay (see Appendix B),

$$C(t_C) = \exp \left[ -D \left( \frac{t_C}{2} - \frac{T_2^{*2} D}{2} \tanh \frac{t_C}{T_2^{*2} D} \right) - \frac{t_C}{\tau_l} \right], \quad (1)$$

where the first part describes irreversible dephasing, which is modeled in a similar manner as in Ref. [16, 31], assuming a realistic Lorentzian noise spectrum. It is quantified by a noise amplitude  $D$  and the reversible coherence time  $T_2^*$  introduced above. The second term accounts for the effective circular state lifetime  $\tau_l$ . A fit to the data over the free parameters  $D$  and  $\tau_l$  reveals  $\tau_l = 1.4(6)$  ms, which is in good agreement with results obtained from detailed measurements of the qubit lifetime below (see Sec. V). The irreversible coherence time ( $C(T_2) = C(0)/2$ ) is derived from the fit function to  $T_2 = 278(10)$   $\mu$ s.

For all the measurements so far, the optical tweezer depth has been set to zero during circular state preparation and probing, i.e. the circular Rydberg qubit was not trapped during the measurements but was slowly dispersing freely in the trapping region. In the following, we keep the tweezer light on to demonstrate trapping of the circular Rydberg states and to quantify the degree of trap-light-induced qubit decoherence.

#### IV. TWEEZER TRAPPING

The trapping potential seen by the circular Rydberg atom is a sum of two contributions, as depicted in Fig. 3(a). First, the driven motion of the Rydberg electron in the oscillating laser field results in a spatially dependent ponderomotive energy shift [32]. For circular Rydberg orbitals similar or smaller in size than the waist of the optical tweezer, this yields a repulsive potential expelling the Rydberg atom from the trap focus (blue dashed line in Fig. 3(a)). As a consequence, optical trapping of alkali (circular) Rydberg atoms, i.e. atoms with a single valence electron, requires tailored bottle beam potentials with a light intensity minimum at the center [19, 33]. Notably, for very high- $n$  circular Rydberg states, with a radius that exceeds the trap waist, the ponderomotive potential develops a central minimum even for Gaussian beam tweezers, allowing to pin circular orbits via the ponderomotive force alone. For our trap waist, this 'needle-trap' effect is expected for circular states with  $n \gtrsim 100$  (red dashed line in Fig. 3(a)) [34]. Alkaline-earth Rydberg atoms feature additional AC polarizability due to the optically active ionic core, resulting in the second contribution to the net trapping potential. For our tweezer wavelength, this results in a strong attractive potential (dotted line in Fig. 3(a)), which overcomes the repulsive ponderomotive force and

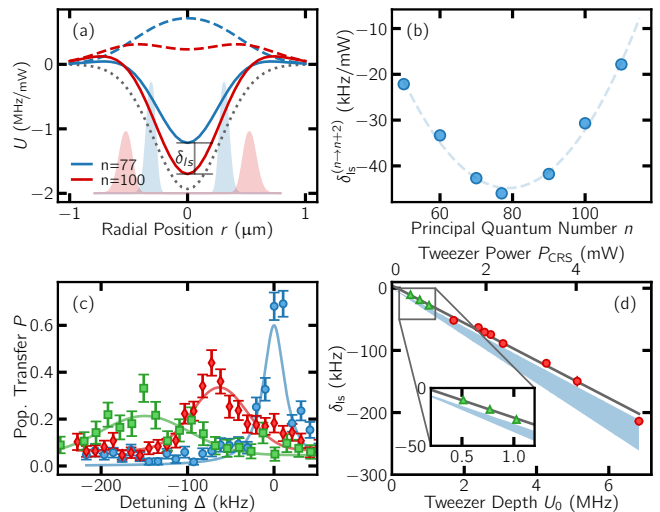


FIG. 3. (a) Radial cut through the calculated tweezer potential for CRS with  $n = 77$  (blue) and  $n = 100$  (red) at the trap center. The dashed lines show the contribution from the ponderomotive potential of the electron in the CRS, and the gray dotted line depicts the contribution from the ionic core polarizability. The size of the electron wavefunction (shaded areas) is comparable to the tweezer waist. The total trap potential (solid lines) depends on  $n$ , leading to a differential light shift  $\delta_{ls}$ . (b) Differential light shift  $\delta_{ls}$  for the two-photon MW transition  $|nC\rangle \rightarrow |(n+2)C\rangle$  as a function of  $n$ . (c) Measured microwave spectrum  $|79C\rangle \rightarrow |77C\rangle$  for tweezer depth  $U_0 = 2.39$  MHz (red diamonds) and  $U_0 = 5.13$  MHz (green squares), compared to the free-space resonance (blue circles). Solid lines are Gaussian fits to the data to extract the light shift. Linewidths are dominated by power broadening from different microwave powers, set for the three measurements. (d) Light shift  $\delta_{ls}$  as a function of tweezer depth  $U_0$  (tweezer power  $P_{CRS}$ ) obtained from microwave spectroscopy data as in (c) (red circles) and from Ramsey oscillations as in Fig. 4 (green triangles). The blue shaded area is an ab-initio calculation of the expected light shift including experimental uncertainties in the tweezer power, while the gray line is a linear fit to the data. In all panels, vertical error bars represent one standard deviation.

readily allows for trapping in a standard Gaussian beam tweezer.

Specifically, the net potential depth  $U_0$  for our  $|79C\rangle$  is about  $1/5$  of the potential seen by the  $^1S_0$  electronic ground state. To ensure qubit trapping in our experiment, we now switch the tweezer light back on immediately after the optical F-state excitation and set the power  $P_{CRS}$  in each tweezer spot to a value at least 6 times larger ( $\approx 350$   $\mu$ W) than the value set for trapping  $^1S_0$  [35]. Note that we did not observe any effect of the trapping potential on the circular state preparation efficiency in our measurements.

In a first set of experiments, we measure the differential light shift of our trapped circular Rydberg qubit over a range of tweezer depths. To this end, we slowly (within 50  $\mu$ s) ramp the tweezer power to larger values up to  $P_{CRS} \approx 5.4$  mW after preparing  $|79C\rangle$ , and then perform



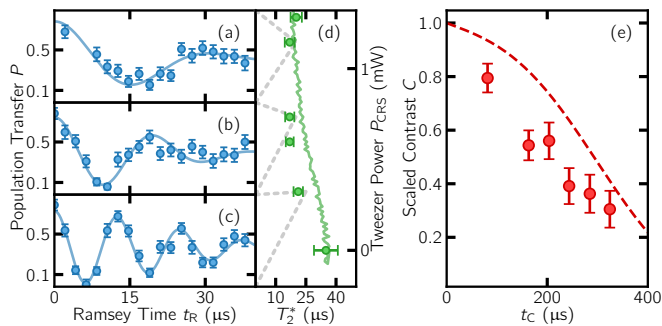


FIG. 4. (a)-(c) Ramsey signal for three different values of the tweezer power  $P_{\text{CRS}} = (1.15, 0.73, 0.32)$  mW. For increasing power the frequency decreases by the tweezer-induced light shift. (d) Reversible coherence time  $T_2^*$  extracted from Ramsey measurements as a function of tweezer power  $P_{\text{CRS}}$  (green circles), compared to expectations from a semi-classical dephasing model (green line). The gray dashed lines mark the correspondence to the Ramsey data in (a)-(c). (e) Spin-echo contrast obtained with the same method as in Fig. 2 (b) but for atoms trapped in tweezers with  $P_{\text{CRS}} = 0.32$  mW (red circles). The red dashed line shows the model fitted to the non-trapped case (Fig. 2(b)) for comparison. Error bars show one standard deviation.

in-trap microwave spectroscopy on the  $|77C\rangle \leftrightarrow |79C\rangle$  qubit transition. Exemplary spectra are depicted in Fig. 3(c), revealing a clear trap-induced light shift on the microwave resonance  $\delta_{\text{is}} < 0$ . Specifically, the tweezer potential is slightly deeper for  $|79C\rangle$  due to the reduced ponderomotive potential (*cf.* solid lines in Fig. 3(a)). This causes a red shift of the qubit resonance in the trap center with respect to the free-space microwave transition ( $\delta_{\text{is}} < 0$ ). In Fig. 3(d) the light shift which is extracted from the center value of Gaussian fits to the data is shown as a function of  $P_{\text{CRS}}$  (red circles). We find good agreement with *ab-initio*  $n$ -dependent trap depth calculations (blue-shaded area). Residual discrepancies are attributed to thermal motion in the trap, for which the atom does not ideally probe the trap bottom.

We also record that the differential light shift is significantly  $n$ -dependent and for our tweezer waist maximal around the principal quantum numbers used throughout this work (see Fig. 3(b)). This can be used for local microwave addressing, at the expense of enhanced motional dephasing.

In a second set of experiments, we repeat the Ramsey and spin-echo experiments from above, but now with trapped circular Rydberg atoms. Exemplary Ramsey fringes for three different values of  $P_{\text{CRS}}$  are shown in Fig. 4(a)-(c). We observe that the oscillation frequency of the free induction decay decreases for increasing trap depth. This is attributed to the differential light shift  $\delta_{\text{is}}$  between the two qubit states  $|79C\rangle$  and  $|77C\rangle$ , causing a red shift and thereby reducing the effective detuning during  $t_R$ . The extracted light shifts are added to Fig. 3(d) (green circles), where we find good agreement with the expected values as well as with light shifts extracted

from the spectroscopy measurements.

We also identify a reduction in  $T_2^*$  with increasing tweezer depth (Fig. 4(d)). A comparison with results from a semi-classical simulation of the dephasing dynamics suggests that the decrease in  $T_2^*$  is due to (thermal) motion in the trap (see Appendix C). This motion is dominated by the short trap release in combination with the photon recoil during the  $20 \mu\text{s}$  long Rydberg F-state excitation. Increasing the currently limited Rydberg laser power and thereby shortening the release duration, should allow us to significantly reduce this source of dephasing. Perspectively, one may also compensate the differential light shift on the qubit by combining the Gaussian trap with a second Laguerre-Gaussian beam with radial index  $p = 0$ , which counteracts the light intensity gradient around the circular electron orbit. Interestingly, using a pair of Laguerre-Gaussian modes with azimuthal index opposite in sign would allow for locally driving transitions between distant circular states [14].

Notably, also the trap-induced dephasing can be rephased via spin-echo (see Fig. 4(e)), though with a slight reduction of the irreversible transverse coherence time compared to the free-space scenario (dashed line in Fig. 4(e)).

## V. LIFETIME

Finally, we investigate the lifetime of our circular Rydberg qubit in more detail. To this end, we initialize the qubit either in  $|79C\rangle$  or  $|77C\rangle$ , the latter via a microwave  $\pi$ -pulse applied after preparing  $|79C\rangle$ . For both scenarios, we hold the atoms in shallow tweezers ( $\approx 400 \mu\text{W}$ ) for a variable time  $t$  and subsequently perform state-selective field ionization. This allows us to identify black-body induced population transfer into neighboring  $n$ -manifolds. Representative histograms of the field-ionization signal are depicted in Fig. 5(c) and (d) at  $t \approx 630 \mu\text{s}$  (indicated by dashed vertical lines) when starting in either of the qubit states. Evidently, decay from the circular state appears to be significantly slower for  $|79C\rangle$ . For a quantitative analysis, we fit the histograms for each hold time with a sum over multiple skewed Gaussians with the individual amplitudes as only free parameters and extract the time-dependent state population  $p_n$  from the areas under the individual curves. Results are depicted in Fig. 5(a) and (b), and allow for extracting lifetimes  $\tau_{|nC\rangle}$  by fitting the data with a rate model (see Appendix E). Specifically, we obtain  $\tau_{|79C\rangle} = 2.55(10)$  ms and  $\tau_{|77C\rangle} = 0.53(8)$  ms. Comparing these observations to predictions in free space at room temperature ( $\tau_{|79C\rangle, \text{fs}} = 303 \mu\text{s}$  and  $\tau_{|77C\rangle, \text{fs}} = 297 \mu\text{s}$ ), we find an enhancement in lifetime by factors of 8.4 and 1.8, respectively. The long circular state lifetimes are attributed to the presence of the ITO electrodes forming a plate capacitor in the  $x$ - $y$  plane, which coincides with the orbital plane of the Rydberg electron. The capacitor plates are spaced by  $d = 10.0(2)$  mm, which is slightly smaller

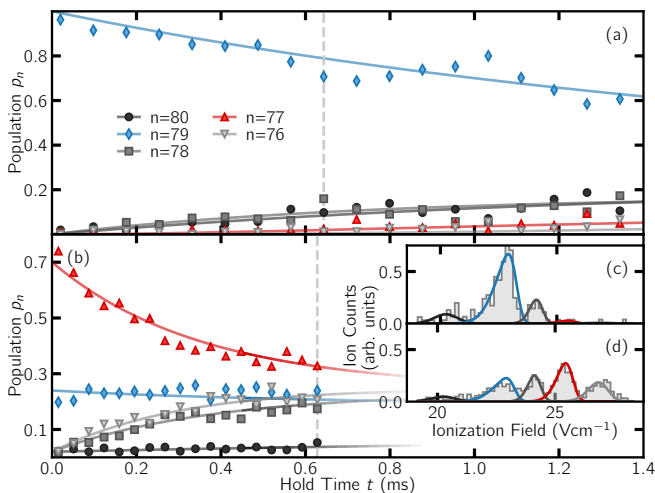


FIG. 5. Decay dynamics of  $|79C\rangle$  (a) and  $|77C\rangle$  (b) into neighboring circular Rydberg states. Symbols depict the populations  $p_n$  in different  $n$ -manifolds as a function of hold time  $t$ . The populations in each state are recorded via SSFI with a  $24 \mu\text{s}$  long linear ionization ramp to  $27(5) \text{ Vcm}^{-1}$ , at various values of  $t$  and are extracted by fitting multiple skewed Gaussians to the obtained ion histograms. The initial population  $p_{77}$  and  $p_{79}$  in (b) arises from the preparation efficiency of  $|77C\rangle$  via a MW  $\pi$ -pulse from  $|79C\rangle$ . Solid lines depict a fit of a rate model to the data, which yields lifetimes for  $|79C\rangle$  ( $|77C\rangle$ ) of  $2.55(10) \text{ ms}$  ( $0.53(8) \text{ ms}$ ). Insets (c) and (d) show representative ion histograms for the datasets in (a) and (b), respectively, recorded at values of  $t$  marked by the dashed vertical lines. The colors indicate the principal quantum numbers labeled in (a) and apply to all subfigures.

than the half-wavelength of black-body transitions into the neighboring  $n$ -manifolds  $\lambda_{\text{BB}}^{n \rightarrow n-1}/2 = 10.6$  ( $10.2$ ) mm for  $|79C\rangle$  ( $|77C\rangle$ ). This leads to suppression of the most detrimental circularly polarized black-body modes inside the electrode structure and allows us to create and control long-lived circular states without cryogenic cooling. The fact that the capacitor spacing is only slightly larger than the relevant black-body wavelength leads to the large difference in suppression factors we find for the two circular qubit states. We find good agreement with calculations for a infinite plate capacitor along the lines of [17], yielding  $\tau_{|77C\rangle} = 0.56 \text{ ms}$  and  $\tau_{|79C\rangle} = 2.37 \text{ ms}$  when assuming a capacitor spacing of  $d = 10.15 \text{ mm}$  and plate reflectivity of  $R = 0.96$ . As the lifetime is extremely sensitive to the capacitor spacing in this regime, measurements at higher  $n$  and a simulation of our finite electrode geometry is necessary to fully characterize the suppression effect. Nevertheless, our calculations suggest that lifetimes  $>10 \text{ ms}$  should be reached when increasing  $n$  to  $\geq 96$ .

## VI. CONCLUSION AND OUTLOOK

We have demonstrated creation and trapping of alkaline-earth atoms in very high- $n$  circular Rydberg states by applying radio-frequency driven adiabatic state preparation to a record-breaking principal quantum number of  $n = 79$ . Trapping in a standard Gaussian tweezer beam is possible due to the core polarization of the divalent Rydberg atom. We implemented microwave control of a circular Rydberg atom qubit and characterized qubit coherence via Ramsey and spin-echo spectroscopy, including analysis of trap-induced dephasing. Our results show coherence times up to  $278(10) \mu\text{s}$ , limited by residual magnetic field noise and electric field gradients in our current setup. Assisted by an in-vacuum suppression capacitor for black-body modes, we find that the produced circular states live for up to  $2.5 \text{ ms}$ , which to the best of our knowledge is the longest-lived Rydberg atom ever observed in a room temperature environment.

Our work opens the door to quantum simulations with alkaline-earth circular Rydberg states, and provides prospects for novel qubit concepts in gate-based Rydberg quantum computers [13, 14, 17]. Higher preparation fidelities or partial-ionization methods to purify the created circular Rydberg states [36] will allow us to decrease the electric field we applied here to separate transitions of nearby elliptical states, which drastically decreases electric field sensitivity. Together with improved magnetic field noise cancellation, this should allow for reaching qubit coherence in the millisecond range and beyond [17], which provides exciting opportunities to overcome fundamental lifetime limitations in state-of-the-art quantum simulators using low- $l$  Rydberg states by orders of magnitude. Specifically, the high- $n$  circular states we demonstrate here give  $> 10 \text{ MHz}$  exchange coupling between neighboring  $n$ , and thus on the order of  $10^4 - 10^5$  coherent flip-flops within their lifetime even at room temperature. Perspectively, reaching two-body gate-fidelities beyond 99.9% would also profit from increased Rydberg state lifetime, at the expense of additional challenges associated with using circular states for digital mode operation [14]. The available ionic-core transitions can be exploited in future experiments for optical read-out and laser cooling of circular Rydberg atoms [37–39]. Narrow-line spectroscopy on the  $\text{Sr}^+$  core also enables coherent and local optical manipulation of the circular state qubit mediated by the electrostatic coupling between the two electrons [27].

Next obvious steps include the creation and control of interacting circular Rydberg atoms, scaling the system to large qubit arrays, possibly assisted by rapid Rabi coupling to circular states [40], and optimal control techniques for improving state preparation efficiencies [41, 42]. Moreover, dynamical rearrangement of the Rydberg atoms within their long lifetime is in reach, and together with non-destructive state detection [27], e.g. via low- $l$  ancilla atoms [14], could be used for filling defects in the array. The long coherence times may then

be used to extend simulations of quantum magnets to situations with strong spin-phonon coupling [43–45], and additional control of radio-frequency coupling to other high- $l$  states in the giant Rydberg manifold provides access to large-spin Heisenberg models [46].

## ACKNOWLEDGMENTS

We thank the **QUANTUM LÄND** team for fruitful discussions and Jennifer Krauter for proofreading. We acknowledge funding from the Federal Ministry of Education and Research (BMBF) under the grants CiRQus and QRydDemo, the Carl Zeiss Foundation via IQST, the Horizon Europe programme HORIZON-CL4-2021-DIGITAL-EMERGING-01-30 via the project 101070144 (EuRyQa), and the Vector Foundation.

## Appendix A: Circularization

In this section we provide additional detail for the adiabatic circularization method described in the main text. By coupling the lowest lying states of each  $m$ , the initial optically accessible F-state can be coupled to the circular Rydberg state. To optimize the adiabatic multi-crossing efficiency when sweeping the electric field, the frequency of all involved transitions must be approximately equal  $f_{m,m+1} \approx f_{\text{RF}}$ . Fig. 6(a) shows those frequencies, calculated (using [47]) with the quantum defects reported in [48] as a function of the electric field and magnetic field of  $B = 0.4 \text{ G}$ . The  $m \leq 3$  states are split-off from the equally spaced hydrogenic manifold with  $m \geq 4$  by the quantum defect. While the transition frequencies  $f_{2,3}$  and  $f_{3,4}$  attach smoothly to the transition frequency of the hydrogenic manifold  $f_{\text{HM}}$  with increasing electric field, the lower- $m$  states get further shifted by states of the neighboring  $n = 78$  manifold, decreasing the transition frequency below  $f_{\text{HM}}$ . The electric field during the ARP must be chosen close to the point where the transition frequency from the initial  $m = 2$  state  $f_{2,3}$  is close to  $f_{\text{HM}}$ , while keeping  $f_{1,2}$  out of resonance to prevent malicious population transfer to states with  $m < 2$ . Note that the calculated crossing point is at  $E = 0.43 \text{ Vcm}^{-1}$  whereas we find it to be between  $E = 0.46 \text{ Vcm}^{-1}$  and  $E = 0.5 \text{ Vcm}^{-1}$  in the experiment. We attribute this to uncertainties in the quantum defects which are measured at  $n = 50$ . In Fig. 6(b), SSFI-traces after the  $t_{\text{ARP}} = 20 \mu\text{s}$  long ARP and a subsequent microwave transfer from  $|79\text{C}\rangle$  to  $|77\text{C}\rangle$  for varying RF voltage amplitudes applied to the circular electric field electrodes is shown. For low amplitudes  $< 6 \text{ mV}$  the emergent avoided crossing is too weak and (partial) diabatic crossing to states with  $m < n - 1$  occurs. For amplitudes between  $6 \text{ mV}$  and  $12 \text{ mV}$  a clear, robust transfer to the  $|77\text{C}\rangle$  is visible, indicating a high success rate of the ARP. If the amplitude is chosen even higher, the transfer efficiency suddenly drops drastically. This can be explained by a

coupling to the  $m = 0, 1$  states, if the split-off frequency  $|f_{1,2} - f_{\text{RF}}|$  from the  $m \geq 4$  states gets comparable to the Rabi frequency of the RF-drive, leading to population transfer to those states.

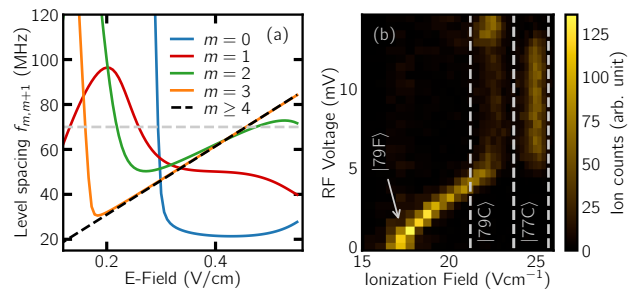


FIG. 6. (a) Calculated transition frequency  $f_{m,m+1}$  between the lowest  $m$  states of the  $n = 79$  hydrogenic manifold of  $^{88}\text{Sr}$  used in the circularization process. The gray-dashed line indicates the RF-frequency  $f_{\text{RF}} = 70 \text{ MHz}$  used in the experiment. (b) RF Voltage dependence of the transfer from  $|79\text{F}\rangle, m = 2\rangle$  to  $|77\text{C}\rangle$ . The SSFI traces are recorded with the same linear ionization ramp as in Fig. 1(d), after the ARP to  $|79\text{C}\rangle$  and a subsequent MW  $\pi$ -pulse resonant with the  $|79\text{C}\rangle$  to  $|77\text{C}\rangle$  transition.

Since the circularization parameters are very sensitive to the F-state attaching to the manifold, the quantum defects are likely not accurate enough to find the optimal parameters. We therefore propose that the preparation fidelity can be strongly increased from the currently 70 % by an in-depth optimization, preferably guided by optimal control methods. Since the parameter space including all electric, magnetic and radio frequency fields is very high-dimensional we leave this for future work. Perspectively, we expect to reach also preparation times on the order of 100 ns and fidelities of 99 % by optimal control assisted coherent excitation as reported in [42] for lower  $n$ .

## Appendix B: Modeling Qubit Decoherence

This section details the decoherence model we use to evaluate the spin-echo measurements of Fig. 2. Our method is similar to the approach in Ref. [16, 31] with an additional term to include the longitudinal, finite-lifetime-induced decay. Specifically, we consider the superposition state

$$|77\text{C}\rangle + e^{i(\phi_0 + \phi_i(t))} |79\text{C}\rangle, \quad (\text{B1})$$

being affected by an acquired non-deterministic phase contribution  $\phi_i(t)$ , which fluctuates differently for each experimental run  $i$ . For a spin-echo experiment,  $\phi_i(t)$  arises from time-dependent fluctuations of the qubit resonance frequency, and is connected to associated fluctuations of

the microwave detuning  $\Delta_0 + \Delta_i(t)$  via

$$\phi_i(t) = - \int_0^{t_R} \Delta_i(t') dt' + \pi + \int_{t_R}^t \Delta_i(t') dt', \quad (\text{B2})$$

assuming of a perfect  $\pi$ -pulse at  $t = t_R$ .

We model the detuning noise  $\Delta_i(t)$  assuming Gaussian white noise  $W(t)$  with amplitude  $D$  and filtered by an exponential decay

$$\Delta_i(t) = \int_{-\infty}^t W_i(t') \frac{\exp\left(\frac{t'-t}{\tau}\right)}{\tau} dt', \quad (\text{B3})$$

where  $\tau$  denotes the correlation time of the resulting noise function. Note that the exponential decay results in a Lorentzian noise spectrum, reflecting the low pass character of magnetic field noise in the experimental setup.

Under these assumptions, the phase variable  $\phi_i(t)$  is normally distributed over the ensemble of experimental realizations with variance  $\sigma^2(t) = \langle \phi_i^2(t) \rangle$ , and results in a Gaussian-like decay of the echo contrast

$$C(t) = e^{-t/\tau_l} \left\langle \Re \left( e^{-i\phi_i(t)} \right) \right\rangle = e^{-\frac{1}{2}\sigma^2(t) - t/\tau_l}, \quad (\text{B4})$$

where we now also include the effective qubit lifetime  $\tau_l$ .

Expressing  $\sigma$  in terms of the noise parameters  $D$  and  $\tau$ , it is straightforward to show, that the maximum of the contrast,  $\partial_t C(t)|_{t_C} = 0$ , is found at

$$t_C = \tau \log \left[ \frac{D\tau_l (2 \exp(t_R/\tau) - 1)}{2 + D\tau_l} \right]. \quad (\text{B5})$$

Notably, this expression is always smaller than  $2t_R$ , shifting the maximum contrast to times earlier than given by  $t_E = t_R$ . This shift is directly evident in the experimental data of Fig. 2. If we assume that the reversible decay is much faster than the effective qubit lifetime  $T_2^* \ll \tau_l$ , and therewith the contrast time shift is dominated by the noise we can approximate Eq. (B5) to

$$t_C \approx \tau \log [2 \exp(t_R/\tau) - 1]. \quad (\text{B6})$$

Here we use that the noise parameters and the reversible coherence time are intimately connected via  $\tau = 1/2DT_2^{*2}$ , which is found from a similar analysis of the Ramsey signal in absence of the echo. Finally, evaluating (B4) at the time of maximal contrast  $t = t_C$  results in

$$C(t_C) = \exp \left[ -D \left( \frac{t_C}{2} - \tau \tanh \left( \frac{t_C}{2\tau} \right) \right) - \frac{t_C}{\tau_l} \right]. \quad (\text{B7})$$

This allows us to fit the experimental data in Fig. 2(b) with Eq. (1), using  $T_2^*$  as obtained from the Ramsey measurement (*cf.* Fig. 2(a)).

With the qubit transition sensitive to magnetic and electric fields, we identify four possible decoherence sources to the  $T_2^*$  time: temporal fluctuations and spatial gradients, both in the electric and magnetic field.

From independent Rydberg F-state spectroscopy at varying electric fields in single tweezers, we find an upper bound for electric field fluctuations of  $\delta_E = 50 \mu\text{V}/\text{cm}$ . With a sensitivity of the  $|79\text{C}\rangle \rightarrow |77\text{C}\rangle$  transition of  $\xi_E = 2\pi \times 8.8 \text{kHz}(\text{mV}/\text{cm})^{-1}$  at the electric control field of  $E = 2 \text{V}/\text{cm}$  used throughout this work, we find a variance of the effective noise-induced detuning of

$$\sigma_E = \xi_E \delta_E \approx 2\pi \times 0.44 \text{kHz}. \quad (\text{B8})$$

From similar spectroscopy measurements, we find that the electric field gradient across the tweezer array is  $\Delta_E = 1.1 \text{mV}/\text{mm}^2$ . The gradient causes a discrete, constant detuning on each tweezer, for which the variance can be obtained from the sum over all tweezer sites  $k$

$$\sigma_{\Delta_E}^2 = \frac{1}{10} \sum_{k=0}^9 (kd\Delta_E\xi_E - \mu_E)^2 = (2\pi \times 2.8 \text{kHz})^2, \quad (\text{B9})$$

with the mean  $\mu_E = \frac{1}{10} \sum_{k=0}^9 (kd\Delta_E\xi_E)$  and the distance between tweezers  $d = 10 \mu\text{m}$ . Analogously, we obtain  $\sigma_{\Delta_B} = 2\pi \times 20 \text{mHz}$  for a magnetic field gradient of  $\Delta_B = 26 \text{mG}/\text{cm}$  we find in our experiment and a magnetic sensitivity of the transition of  $\xi_B = 2\pi \times \delta_m \mu_B$  with  $\delta_m = 2$  the difference in magnetic quantum number  $m$ , and  $\mu_B = 1.4 \text{MHz}/\text{G}$ . Evidently, decoherence by magnetic field gradients and electric field fluctuations are orders of magnitude smaller than the influence of the electric field gradient and can be neglected. Assuming uncorrelated noise sources, the  $T_2^*$  time is directly connected to the summed variances via

$$\frac{1}{T_2^{*2}} = \sigma_{\Delta_E}^2 + \sigma_B^2. \quad (\text{B10})$$

With the measured  $T_2^*$  time we can give an approximate value for the magnetic field noise by solving Eq. B10 for  $\sigma_B$ . We find  $\sigma_B = 2\pi \times 2.4 \text{kHz}$  on the same order as the electric field gradient induced noise. This corresponds to magnetic field fluctuations of  $\delta_B \approx 0.9 \text{mG}$ , comparable with values we find from independent measurements of the microwave transition resonance.

### Appendix C: Semi-Classical Simulation of Trap-Induced Dephasing

In this section we provide details on the semi-classical analysis of the dephasing induced by motion of the atom in the tweezer potential shown in Fig. 4. The dominating source of motion is the heating due to the short switch-off of the tweezer light for Rydberg laser excitation during which 461 nm photons are scattered. The scattering rate of the two upper Rydberg photons (768 nm and 893 nm) can be neglected since the transferred momentum and the scattering rate is much lower in our setup. We start the simulation by drawing a Monte Carlo sample of the ground state atoms position and velocity vectors in a harmonic potential from a classical thermal distribution.



Guided by earlier measurements in [28], we approximate the initial temperature to  $T \approx 15 \mu\text{K}$ . We then calculate the atoms position and velocity after evolution in free space for the  $20 \mu\text{s}$  long Rydberg excitation, during which it absorbs between one and two  $461 \text{ nm}$  photons at random times. After the Rydberg excitation, quenching on the trapping potential to a variable depth  $U_0$  leads to a kick of the atom dependent on its position and velocity. The resulting motion leads to a time-dependent light shift experienced by the atom, altering the detuning during the Ramsey sequence. This is included into the two-level atom Hamiltonian describing the qubit evolution during the Ramsey sequence by a time-dependent detuning. By solving the von Neumann equation numerically for each Monte Carlo sample, we obtain the temporal evolution of the qubit states. By fitting a Gaussian envelope to the result, the  $T_2^*$  time is extracted for different tweezer powers  $P_{\text{CRS}}$  which is plotted in Fig. 4.

## Appendix D: Trapping Potential Calculation

### 1. $\text{Sr}^+$ Ionic Core Potential

To calculate the trapping potential for the ionic core we use a sum-over-states method [49]

$$U(\vec{r}) = -\frac{3\pi c^2}{2\omega_0^3} \sum_k \left( \frac{\Gamma_k}{\omega_0 - \omega_k} + \frac{\Gamma_k}{\omega_0 + \omega_k} \right)^2 I(\vec{r}), \quad (\text{D1})$$

where  $\omega_0$  is the frequency of the trapping laser and  $I(\vec{r}) = I(r, z)$  the position-dependent tweezer intensity. The index  $k$  iterates over all optical dipole transitions with linewidth  $\Gamma_k$  and frequency  $\omega_k$  connected to the electronic ground state  $5s^2S_{1/2}$  listed in [50]. We assume the tweezer to be of Gaussian form at the position of the focus with

$$I(r, z) = \frac{2P_0}{\pi w(z)^2} \exp\left(-\frac{2r^2}{w(z)^2}\right), \quad (\text{D2})$$

where  $w(z)$  is the spot size parameter and  $P_0$  the laser power.

### 2. Ponderomotive Potential

The ponderomotive potential for the Rydberg electron shown in Fig. 3 (a) is that of a free electron [51] defined as

$$U_p(\vec{r}) = \frac{e^2}{2m_e c \epsilon_0 \omega_0^2} \int I(\vec{r}' + \vec{r}) |\Psi(\vec{r}')|^2 d^3r', \quad (\text{D3})$$

where  $\Psi(\vec{r})$  is the circular state wavefunction. The integration is then carried out numerically.

## Appendix E: CRS Decay-Rate Model

To measure the lifetimes of the CRS we perform SSFI with a  $24 \mu\text{s}$  long linear electric field ramp to  $\approx 28 \text{ Vcm}^{-1}$  after a variable hold time  $t$ . The so obtained histograms (see Fig. 5 (c),(d)) have a high resolution in the ionization field range between  $20 - 27 \text{ Vcm}^{-1}$ , allowing for the distinction of CRS with neighboring principal quantum number  $n$  with  $76 \leq n \leq 80$ . Non-circular states with the same  $n$  are counted to the corresponding CRS since they have very similar ionization threshold fields and can not be distinguished with SSFI. This will not influence the prime results of this analysis since the decay rates are orders of magnitude smaller than the black-body induced transfer between CRS [13].

To obtain the state populations  $p_n$  from the histograms, we find that a sum of skewed Gaussians of the form

$$\sum_{n=76}^{80} A_n \frac{2}{\sigma_n 2\pi} e^{-\frac{(E-E_n^0)^2}{2\sigma_n^2}} \int_{-\infty}^{(E-E_n^0)\alpha/\sigma_n} e^{-\frac{E'^2}{2}} dE', \quad (\text{E1})$$

with the skew factor  $\alpha$  approximates the form of the histograms reasonably well. Here,  $E_n^0$  ( $\sigma_n$ ) is the center field (width) of each Gaussian. The individual amplitudes  $A_n$  are normalized to obtain the state populations  $p_n = A_n / \sum_m A_m$ . Since the different CRS have a finite overlap in the ion histograms, it is not feasible to fit Eq. (E1) over all parameters. Instead a stepwise procedure is necessary. First, for  $|79C\rangle$  and  $|77C\rangle$  at  $t = 0$  a histogram where the corresponding state is dominant is measured and fitted with a single skewed Gaussian. Then the width  $\sigma_n$  and position  $E_n^0$  are fixed and only the population  $p_n$  is used as free parameter in the following fits. With the same procedure one state after the other is added to the sum, fixing all  $\sigma_n$  and  $E_n^0$ , leaving the populations  $p_n$  the only free parameters.

The black-body-induced transfer between adjacent CRS can be described by a classical rate model [18]. Each atom in  $|nC\rangle$  has a certain chance to be transferred either up or down by one  $n$  to  $|(n \pm 1)C\rangle$  with rate  $\gamma_{n \rightarrow n \pm 1}$ . Since the amount of black-body photons with  $f \approx 13.9 \text{ GHz}$  is large at room temperature, we can assume  $\gamma_{n \rightarrow m} = \gamma_{m \rightarrow n}$ . The change in population  $\dot{p}_n$  is then governed by the transfer out of the state but also by the transfer from neighboring states into it, yielding

$$\begin{aligned} \dot{p}_n = & -(\gamma_{n \rightarrow n+1} + \gamma_{n \rightarrow n-1}) p_n \\ & + \gamma_{n-1 \rightarrow n} p_{n-1} + \gamma_{n+1 \rightarrow n} p_{n+1}. \end{aligned}$$

We limit the differential equation to the experimentally accessible states  $76 \leq n \leq 80$  by setting  $\gamma_{81 \rightarrow 80} = \gamma_{75 \rightarrow 76} = 0$ . This system of differential equations is then solved analytically and fitted over the decay rates  $\gamma_{n \rightarrow m}$  to the data shown in Fig. 5 to obtain lifetimes  $\tau_n = 1/(\gamma_{n \rightarrow n+1} + \gamma_{n \rightarrow n-1})$ .

- [1] A. Browaeys and T. Lahaye, Many-body physics with individually controlled rydberg atoms, *Nature Physics* **16**, 132 (2020).
- [2] P. Scholl, M. Schuler, H. J. Williams, A. A. Eberharter, D. Barredo, K.-N. Schymik, V. Lienhard, L.-P. Henry, T. C. Lang, T. Lahaye, A. M. Läuchli, and A. Browaeys, Quantum simulation of 2d antiferromagnets with hundreds of rydberg atoms, *Nature* **595**, 233 (2021).
- [3] S. Ebadi, T. T. Wang, H. Levine, A. Keesling, G. Semeghini, A. Omran, D. Bluvstein, R. Samajdar, H. Pichler, W. W. Ho, S. Choi, S. Sachdev, M. Greiner, V. Vuletić, and M. D. Lukin, Quantum phases of matter on a 256-atom programmable quantum simulator, *Nature* **595**, 227 (2021).
- [4] M. Kim, K. Kim, J. Hwang, E.-G. Moon, and J. Ahn, Rydberg quantum wires for maximum independent set problems, *Nature Physics* **18**, 755 (2022).
- [5] S. Ebadi, A. Keesling, M. Cain, T. T. Wang, H. Levine, D. Bluvstein, G. Semeghini, A. Omran, J.-G. Liu, R. Samajdar, X.-Z. Luo, B. Nash, X. Gao, B. Barak, E. Farhi, S. Sachdev, N. Gemelke, L. Zhou, S. Choi, H. Pichler, S.-T. Wang, M. Greiner, V. Vuletić, and M. D. Lukin, Quantum optimization of maximum independent set using rydberg atom arrays, *Science* **376**, 1209 (2022).
- [6] I. S. Madjarov, J. P. Covey, A. L. Shaw, J. Choi, A. Kale, A. Cooper, H. Pichler, V. Schkolnik, J. R. Williams, and M. Endres, High-fidelity entanglement and detection of alkaline-earth rydberg atoms, *Nature Physics* **16**, 857 (2020).
- [7] T. M. Graham, Y. Song, J. Scott, C. Poole, L. Phuttitarn, K. Jooya, P. Eichler, X. Jiang, A. Marra, B. Grinckemeyer, M. Kwon, M. Ebert, J. Cherek, M. T. Lichtman, M. Gillette, J. Gilbert, D. Bowman, T. Ballance, C. Campbell, E. D. Dahl, O. Crawford, N. S. Blunt, B. Rogers, T. Noel, and M. Saffman, Multi-qubit entanglement and algorithms on a neutral-atom quantum computer, *Nature* **604**, 457 (2022).
- [8] D. Bluvstein, H. Levine, G. Semeghini, T. T. Wang, S. Ebadi, M. Kalinowski, A. Keesling, N. Maskara, H. Pichler, M. Greiner, V. Vuletić, and M. D. Lukin, A quantum processor based on coherent transport of entangled atom arrays, *Nature* **604**, 451 (2022).
- [9] J. W. Lis, A. Senoo, W. F. McGrew, F. Rönchen, A. Jenkins, and A. M. Kaufman, Midcircuit operations using the omg architecture in neutral atom arrays, *Phys. Rev. X* **13**, 041035 (2023).
- [10] W. Huie, L. Li, N. Chen, X. Hu, Z. Jia, W. K. C. Sun, and J. P. Covey, Repetitive readout and real-time control of nuclear spin qubits in  $^{171}\text{Yb}$  atoms, *PRX Quantum* **4**, 030337 (2023).
- [11] S. Ma, G. Liu, P. Peng, B. Zhang, S. Jandura, J. Claes, A. P. Burgers, G. Pupillo, S. Puri, and J. D. Thompson, High-fidelity gates and mid-circuit erasure conversion in an atomic qubit, *Nature* **622**, 279 (2023).
- [12] D. Bluvstein, S. J. Evered, A. A. Geim, S. H. Li, H. Zhou, T. Manovitz, S. Ebadi, M. Cain, M. Kalinowski, D. Hangleiter, J. P. B. Ataiades, N. Maskara, I. Cong, X. Gao, P. S. Rodriguez, T. Karolyshyn, G. Semeghini, M. J. Gullans, M. Greiner, V. Vuletić, and M. D. Lukin, Logical quantum processor based on reconfigurable atom arrays, *Nature* [10.1038/s41586-023-06927-3](https://doi.org/10.1038/s41586-023-06927-3) (2023).
- [13] T. L. Nguyen, J. M. Raimond, C. Sayrin, R. Cortiñas, T. Cantat-Moltrecht, F. Assemat, I. Dotsenko, S. Gleyzes, S. Haroche, G. Roux, T. Jolicœur, and M. Brune, Towards quantum simulation with circular rydberg atoms, *Phys. Rev. X* **8**, 011032 (2018).
- [14] S. R. Cohen and J. D. Thompson, Quantum computing with circular rydberg atoms, *PRX Quantum* **2**, 030322 (2021).
- [15] S. Haroche and J.-M. Raimond, *Exploring the Quantum: Atoms, Cavities, and Photons* (Oxford University Press, 2006).
- [16] T. Cantat-Moltrecht, R. Cortiñas, B. Ravon, P. Méhaignerie, S. Haroche, J. M. Raimond, M. Favier, M. Brune, and C. Sayrin, Long-lived circular rydberg states of laser-cooled rubidium atoms in a cryostat, *Phys. Rev. Res.* **2**, 022032(R) (2020).
- [17] F. Meinert, C. Hölzl, M. A. Nebiöglu, A. D’Arnese, P. Karl, M. Dressel, and M. Scheffler, Indium tin oxide films meet circular rydberg atoms: Prospects for novel quantum simulation schemes, *Phys. Rev. Res.* **2**, 023192 (2020).
- [18] H. Wu, R. Richaud, J.-M. Raimond, M. Brune, and S. Gleyzes, Millisecond-lived circular rydberg atoms in a room-temperature experiment, *Phys. Rev. Lett.* **130**, 023202 (2023).
- [19] B. Ravon, P. Méhaignerie, Y. Machu, A. D. Hernández, M. Favier, J. M. Raimond, M. Brune, and C. Sayrin, Array of individual circular rydberg atoms trapped in optical tweezers, *Phys. Rev. Lett.* **131**, 093401 (2023).
- [20] A. Cooper, J. P. Covey, I. S. Madjarov, S. G. Porsev, M. S. Safronova, and M. Endres, Alkaline-earth atoms in optical tweezers, *Phys. Rev. X* **8**, 041055 (2018).
- [21] M. A. Norcia, A. W. Young, and A. M. Kaufman, Microscopic control and detection of ultracold strontium in optical-tweezer arrays, *Phys. Rev. X* **8**, 041054 (2018).
- [22] J. T. Wilson, S. Saskin, Y. Meng, S. Ma, R. Dilip, A. P. Burgers, and J. D. Thompson, Trapping alkaline earth rydberg atoms optical tweezer arrays, *Physical Review Letters* **128**, 033201 (2022).
- [23] I. S. Madjarov, A. Cooper, A. L. Shaw, J. P. Covey, V. Schkolnik, T. H. Yoon, J. R. Williams, and M. Endres, An atomic-array optical clock with single-atom readout, *Phys. Rev. X* **9**, 041052 (2019).
- [24] A. W. Young, W. J. Eckner, W. R. Milner, D. Kedar, M. A. Norcia, E. Oelker, N. Schine, J. Ye, and A. M. Kaufman, Half-minute-scale atomic coherence and high relative stability in a tweezer clock, *Nature* **588**, 408 (2020).
- [25] S. Ma, A. P. Burgers, G. Liu, J. Wilson, B. Zhang, and J. D. Thompson, Universal gate operations on nuclear spin qubits in an optical tweezer array of  $^{171}\text{Yb}$  atoms, *Phys. Rev. X* **12**, 021028 (2022).
- [26] K. Barnes, P. Battaglino, B. J. Bloom, K. Cassella, R. Coxe, N. Crisosto, J. P. King, S. S. Kondov, K. Kotru, S. C. Larsen, J. Lauigan, B. J. Lester, M. McDonald, E. Megidish, S. Narayanaswami, C. Nishiguchi, R. Notermans, L. S. Peng, A. Ryou, T.-Y. Wu, and M. Yarwood, Assembly and coherent control of a register of nuclear spin qubits, *Nature Communications* **13**, 2779 (2022).
- [27] A. Muni, L. Lachaud, A. Couto, M. Poirier, R. C. Teixeira, J.-M. Raimond, M. Brune, and S. Gleyzes, Optical

- coherent manipulation of alkaline-earth circular rydberg states, *Nature Physics* **18**, 502 (2022).
- [28] C. Hölzl, A. Götzelmann, M. Wirth, M. S. Safronova, S. Weber, and F. Meinert, Motional ground-state cooling of single atoms in state-dependent optical tweezers, *Phys. Rev. Res.* **5**, 033093 (2023).
- [29] Throughout this work, the excitation rate into the F-state is low enough that interactions do not play a role. Limited by laser power, we typically create not more than one Rydberg atom per realization.
- [30] R. C. Teixeira, A. Larrouy, A. Muni, L. Lachaud, J.-M. Raimond, S. Gleyzes, and M. Brune, Preparation of long-lived, non-autoionizing circular rydberg states of strontium, *Physical Review Letters* **125**, 263001 (2020).
- [31] R. G. Cortiñas, *Laser trapped Circular Rydberg atoms for quantum simulation*, Ph.D. thesis, Université Paris sciences et lettres (2020).
- [32] S. K. Dutta, J. R. Guest, D. Feldbaum, A. Walz-Flannigan, and G. Raithel, Ponderomotive optical lattice for rydberg atoms, *Phys. Rev. Lett.* **85**, 5551 (2000).
- [33] D. Barredo, V. Lienhard, P. Scholl, S. de Léséleuc, T. Boulier, A. Browaeys, and T. Lahaye, Three-dimensional trapping of individual rydberg atoms in ponderomotive bottle beam traps, *Phys. Rev. Lett.* **124**, 023201 (2020).
- [34] R. G. Cortiñas, Threading an atom with light, *Phys. Rev. A* **109**, L011102 (2024).
- [35] Clear signatures of trapping are also apparent from the ion arrival times on the MCP. For hold times up to several milliseconds, we observe a shift and broadening for  $P_{\text{CRS}} = 0$ , which is absent for the trapped case.
- [36] R. G. Cortiñas, M. Favier, B. Ravon, P. Méhaignerie, Y. Machu, J. M. Raimond, C. Sayrin, and M. Brune, Laser trapping of circular rydberg atoms, *Phys. Rev. Lett.* **124**, 123201 (2020).
- [37] C. E. Simien, Y. C. Chen, P. Gupta, S. Laha, Y. N. Martinez, P. G. Mickelson, S. B. Nagel, and T. C. Killian, Using absorption imaging to study ion dynamics in an ultracold neutral plasma, *Phys. Rev. Lett.* **92**, 143001 (2004).
- [38] T. K. Langin, G. M. Gorman, and T. C. Killian, Laser cooling of ions in a neutral plasma, *Science* **363**, 61 (2019).
- [39] V. Letchumanan, G. Wilpers, M. Brownnutt, P. Gill, and A. G. Sinclair, Zero-point cooling and heating-rate measurements of a single  $^{88}\text{Sr}^+$  ion, *Phys. Rev. A* **75**, 063425 (2007).
- [40] A. Signoles, E. K. Dietsche, A. Facon, D. Grosso, S. Haroche, J. M. Raimond, M. Brune, and S. Gleyzes, Coherent transfer between low-angular-momentum and circular rydberg states, *Phys. Rev. Lett.* **118**, 253603 (2017).
- [41] S. Patsch, D. M. Reich, J.-M. Raimond, M. Brune, S. Gleyzes, and C. P. Koch, Fast and accurate circularization of a rydberg atom, *Phys. Rev. A* **97**, 053418 (2018).
- [42] A. Larrouy, S. Patsch, R. Richaud, J.-M. Raimond, M. Brune, C. P. Koch, and S. Gleyzes, Fast navigation in a large hilbert space using quantum optimal control, *Physical Review X* **10**, 021058 (2020).
- [43] F. M. Gambetta, W. Li, F. Schmidt-Kaler, and I. Lesanovsky, Engineering nonbinary rydberg interactions via phonons in an optical lattice, *Phys. Rev. Lett.* **124**, 043402 (2020).
- [44] M. Magoni, R. Joshi, and I. Lesanovsky, Molecular dynamics in rydberg tweezer arrays: Spin-phonon entanglement and jahn-teller effect, *Phys. Rev. Lett.* **131**, 093002 (2023).
- [45] P. Méhaignerie, C. Sayrin, J.-M. Raimond, M. Brune, and G. Roux, Spin-motion coupling in a circular-rydberg-state quantum simulator: Case of two atoms, *Phys. Rev. A* **107**, 063106 (2023).
- [46] A. Kruckenhauser, R. van Bijnen, T. V. Zache, M. Di Liberto, and P. Zoller, High-dimensional so(4)-symmetric rydberg manifolds for quantum simulation, *Quantum Sci. Technol.* **8**, 015020 (2022).
- [47] S. Weber, C. Tresp, H. Menke, A. Urvoy, O. Firstenberg, H. P. Büchler, and S. Hofferberth, Calculation of rydberg interaction potentials, *Journal of Physics B: Atomic, Molecular and Optical Physics* **50**, 133001 (2017).
- [48] S. Patsch, *Control of Rydberg atoms for quantum technologies*, Ph.D. thesis (2022).
- [49] R. Grimm, M. Weidemüller, and Y. B. Ovchinnikov, Optical dipole traps for neutral atoms, in *Advances In Atomic, Molecular, and Optical Physics* (Elsevier, 2000) pp. 95–170.
- [50] A. Kramida, Yu. Ralchenko, J. Reader, and NIST ASD Team, NIST Atomic Spectra Database (ver. 5.11), [Online]. Available: <https://physics.nist.gov/asd> [2024, January 4]. National Institute of Standards and Technology, Gaithersburg, MD. (2023).
- [51] B. Knuffman and G. Raithel, Multipole transitions of rydberg atoms in modulated ponderomotive potentials, *Physical Review A* **75**, 053401 (2007).